Numerical Study of the Cold Metal Transfer (CMT) Welding of Thin Austenitic Steel Plates with an Equivalent Heat Source Approach

Hichem Aberbache, Alexandre Mathieu, Nathan Haglon, Rodolphe Bolot, Laurent Bleurvacq, Axel Corolleur, Fabrice Laurent

Journal of
Manufacturing and Materials Processing

MDPI

Article

Numerical Study of the Cold Metal Transfer (CMT) Welding of Thin Austenitic Steel Plates with an Equivalent Heat Source Approach

Hichem Aberbache [1,2,*], Alexandre Mathieu [1], Nathan Haglon [1], Rodolphe Bolot [1], Laurent Bleurvacq [1], Axel Corolleur [2] and Fabrice Laurent [2]

[1] Laboratoire Interdisciplinaire Carnot de Bourgogne, UMR 6303 CNRS, Université de Bourgogne Franche-Comté, 12 rue de la Fonderie, 71200 Le Creusot, France; alexandre.mathieu@u-bourgogne.fr (A.M.); rodolphe.bolot@u-bourgogne.fr (R.B.); ecco.lb@gmail.com (L.B.)
[2] MAGYAR-SMFF, Route de Chazeuil, 21610 Fontaine-Française, France; axel.corolleur@magyar.fr (A.C.); fabrice.laurent@magyar.fr (F.L.)
* Correspondence: hichem.aberbache@u-bourgogne.fr or hichemaberbache@yahoo.fr; Tel.: +33-(0)38-573-1042

Abstract: The CMT (cold metal transfer) arc welding process is a valuable joining method for assembling thin sheets, minimizing heat transfers, and reducing subsequent deformations. The study aims to simulate the CMT welding of thin stainless-steel sheets to predict temperature fields and deformations. Both instrumented tests and numerical simulations were conducted for butt-welding of sheets with a thickness of 1 to 1.2 mm. Weld seam samples were observed to identify equivalent heat sources for each configuration. The electric current and voltage were monitored. Temperature measurements were performed using K-type thermocouples, as well as displacement measurements via the DIC (digital image correlation) technique. Thermomechanical simulations, considering phase changes and the actual seam geometry induced by filler material, were conducted using an equivalent heat source approach. A unique heat exchange coefficient accounting for thermal losses was identified. By incorporating these losses into thermal calculations, a good agreement was found between measured and calculated temperatures. Mechanical calculations allowed for the recovery of the horse saddle form after actual welding, with a relative difference of less than 10% in angular distortion between calculated and measured values.

Keywords: cold metal transfer; welding automation; austenitic stainless-steel; numerical simulation

Citation: Aberbache, H.; Mathieu, A.; Haglon, N.; Bolot, R.; Bleurvacq, L.; Corolleur, A.; Laurent, F. Numerical Study of the Cold Metal Transfer (CMT) Welding of Thin Austenitic Steel Plates with an Equivalent Heat Source Approach. *J. Manuf. Mater. Process.* **2024**, *8*, 20. https://doi.org/10.3390/jmmp8010020

Academic Editor: Ivan Galvão

Received: 26 November 2023
Revised: 18 January 2024
Accepted: 19 January 2024
Published: 26 January 2024

1. Introduction

The present study aims at limiting the weight of welded steel structures in the context of road transport. One way consists of decreasing the thickness of the sheets and avoiding any stiffness loss by applying other means.

Welding operations give rise to deformations and internal stresses that could compromise the durability of the structure. For the sake of balancing the probable stiffness loss, alternative techniques, including reinforcement in the manufacturing of structures, are put forward by the company Magyar. Moreover, numerical simulation of the metal structure assembling process can be conducted in order to forecast the temperature fields and deformations caused by the welding process.

As part of this project, a thermomechanical simulation was performed for the MAG (metal active gas)/CMT (cold metal transfer) welding process applied to structures constructed from thin-walled austenitic stainless-steel sheets. In this context, a comprehensive program of tests and numerical simulations has been outlined, which would permit comparisons between the conducted experiments and corresponding simulations. More specifically, the observation encompasses both the thermal and mechanical phenomena that occur during welding operations.

The experimental aspect of this study focuses on instrumented welding tests that involve sheets with a thickness ranging from 1 to 1.2 mm. This instrumentation primarily encompasses thermal measurements using thermocouples (TC), measurements of welding current and voltage, and acquisition of displacement data to assess sheet deformations through the digital image correlation (DIC) technique. Furthermore, macrograph samples of the weld seams are observed to identify and model the equivalent heat source for welding conditions of 304L stainless-steel grade. The process for establishing these analogous sources is based on experimental measurements of the dimensions and properties of molten zones (MZ), followed by recalibration of the geometric and energy parameters of a pre-set heat source. The provided equivalent heat sources are then incorporated into thermomechanical calculations.

Modeling and simulation of thermal and thermomechanical behaviors were conducted using the ABAQUS commercial computation software, employing sub-programs (DFLUX) coded in FORTRAN to incorporate the heat sources required by this approach.

For these experiments, the CMT welding process introduced by Fronius in 2004 [1] was selected. This process involves the assistance of a mechanical recoil of the wire to facilitate the detachment of the metal droplet. The welding operation is synchronized to ensure the detachment and deposition of the droplet that occurs when the current reaches almost zero (when the electrical resistance R is high) [2].

Several references highlight the advantages of the CMT process, particularly in the context of thin sheets joining [3–6]. In a study conducted by Talalaev et al. [6], the authors discuss the problem of distortion and the deformation of stainless-steel parts with a thickness ranging from 2 to 4 mm during welding. They have demonstrated that a welding velocity V_w in the range of 600–720 mm/min ensures low porosity and minimizes the product distortion. The authors also suggested that the optimization of heat input Q between 70 and 110 J/mm ensures adequate joint penetration while minimizing deformations.

Gas-shielded welding, particularly the CMT process, is highly valuable in industries like automotive, aeronautics, aerospace, and metal production. CMT offers an innovative arc-welding approach suitable for automation. It maintains lower temperatures, enabling the welding of thin metal sheets in an edge-to-edge configuration, but for thicknesses that are not less than 0.3 mm. The key features of the CMT process include a controlled short arc interruption and wire movement integration, resulting in uniform, spatter-free welding. At frequencies of up to 70 Hz, short-circuits occur automatically, reducing current and heat. Compared to traditional MIG (metal inert gas)/MAG welding, CMT offers lower heat input and a stable arc. It is ideal for thin materials, causing minimal damage to the base metal, expanding tolerance ranges, and providing clean welding in any position or speed [7].

Numerical simulations of CMT welding for thin plates have been the subject of investigations in various research endeavors. Researchers have introduced a heat source model designed to replicate the effects of periodic arcing and metal deposition phenomena inherent to the CMT welding process [8]. Leveraging ANSYS software, a numerical simulation model has been used to depict the temperature field within the CMT welding pool, providing a dynamic representation of this process [9]. Furthermore, a 3D transient CMT welding model was created to explore heat and mass transfer dynamics during the CMT welding of aluminum alloy and galvanized mild steel [10]. Notably, a rapid methodology has been proposed for adjusting heat source model parameters, allowing for the accurate reproduction of temperature evolution and distortions in a welded joint [11]. Another work has established a thermomechanical model to predict distortions and residual stresses in metal parts manufactured using this process [12].

2. Experimental Conditions

In the current study, a number of butt-welding tests have been carried out on samples with a thickness ranging from 1 to 1.2 mm. The welded assemblies are composed of two 100 mm × 80 mm stainless-steel sheets. These configurations (including variations in the

thicknesses) were selected to account for the variability of the bottom and shell thicknesses to be welded for the construction of tanks. All MIG/CMT welding experiments were carried out using a FRONIUS CMT 4000 welding generator.

The first specimen consisted of two sheets of equal thickness (1 mm), while the second specimen involved two sheets with different thicknesses, specifically 1.2 mm and 1 mm. To minimize deformation, these two sheets were welded in contact with a copper lath in order to avoid any overheating of the base metal.

Welded sheets were equipped with instrumentation, allowing for the measurement of temperatures both during and after welding. Temperature measurements were performed as close as possible from the weld line and were achieved by fixing K-type thermocouples in the vicinity of the welding area. To safeguard these thermocouples from heat damage during welding, they were shielded by small metal sheets, see Figure 1.

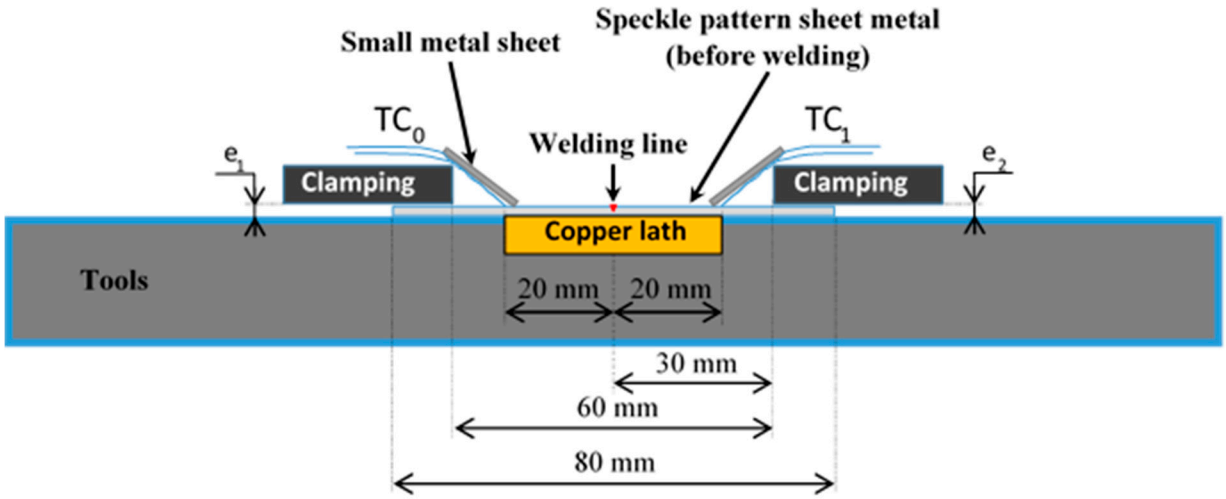

Figure 1. Schematic showing the positioning of thermocouples, protection, clamping, and copper lath.

These two thermocouples (TC_0 and TC_1) were positioned at the center of the sheet, with a 20 mm gap with regard to the welding line, as illustrated in Figure 1. This distance ensured that the thermocouples were not exposed to burning during welding, a situation typically encountered in CMT welding, where the width of the weld seam is more substantial compared to other processes such as TIG (tungsten inert gas) welding.

Clampings were positioned on both sides of the sheet, extending all the way to the ends in both the transverse and longitudinal directions of the sheet, with a 30 mm gap from the weld line. This clamping setup guarantees that both sides of the sheet remain firmly in place during the welding process.

To prevent any misalignment during CMT welding, both coupons were initially Laser spot welded each 25 mm before CMT welding. In addition, LASER technology was used to minimize distortion resulting from this pointing process.

During the CMT processing, a welding speed of 650 mm/min was selected, which is consistent with Talalaev's suggestions [6].

Displacements and deformations caused by welding were measured using the DIC technique [13]. This measurement method involves applying a speckle pattern to the sheet surface before welding. The speckle pattern consists of a white background with random black spots of varying sizes. DIC measurements were executed using VIC3D software (version 2010), see Figure 2.

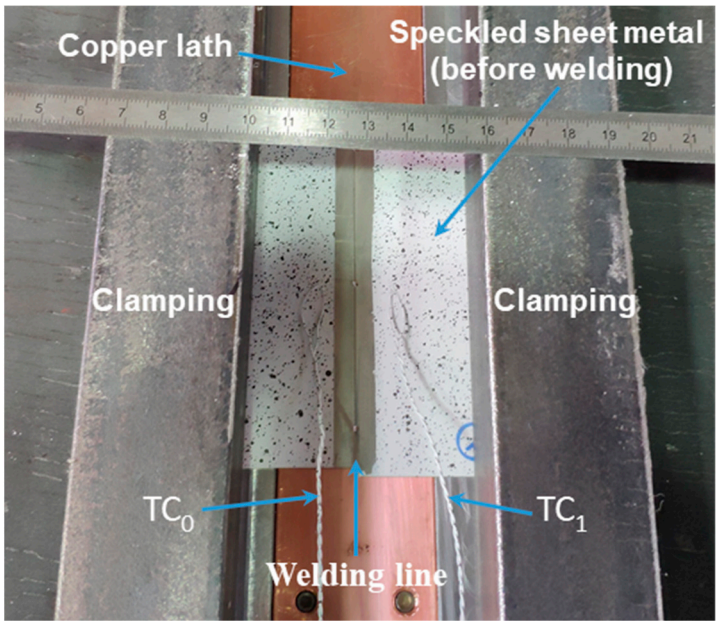

Figure 2. Actual experiment displaying the speckle pattern utilized for the DIC technique.

Figure 1 illustrates the welding process with a copper lath, application of the speckle pattern on metal sheets, thermocouples protected by small metal sheets, and clamping conditions employed during welding experiments. The clamping was maintained during the cooling phase.

Measuring the electric current and voltage values allowed us to obtain a more accurate estimation of the power dissipated within the primary welding circuit.

Indeed, it is important to note that the desired voltage and current parameters may not always be achieved during an arc welding experiment. Various events may transpire during the tests, such as short circuits or oscillations of the bath surface, which may result in an operating point that the generator cannot attain or a change in the transfer mode. All that can lead to alterations in voltage and/or current values.

In electric arc welding, linear welding energy Es is a function of welding speed, effective arc voltage, and current. It is expressed as follows:

$$Es = 60\frac{U\,I}{V_w}\,10^{-3} \quad (1)$$

With: U arc voltage (V); I arc current intensity (A); and V_w (mm/min) to provide Es (kJ/mm).

Determining the welding speed is a straightforward process. When it comes to voltage (U) and current (I), one typically relies on values obtained by averaging several measurements. These measurements can be taken directly from the welding generator if it undergoes periodic checks, or from calibrated external devices. In our studies, current clamps are used to measure I(t) and U(t), displaying the actual (effective) current and voltage (I_{eff} and U_{eff}), as demonstrated in Figure 3.

These devices allow for capturing of U(t) and I(t) with a high acquisition frequency, digitally multiplying the two to derive an instantaneous power value P. This value can be averaged over a specific duration, or it can be used to calculate the total energy E_{tot}, making the determination of welding energy quite straightforward.

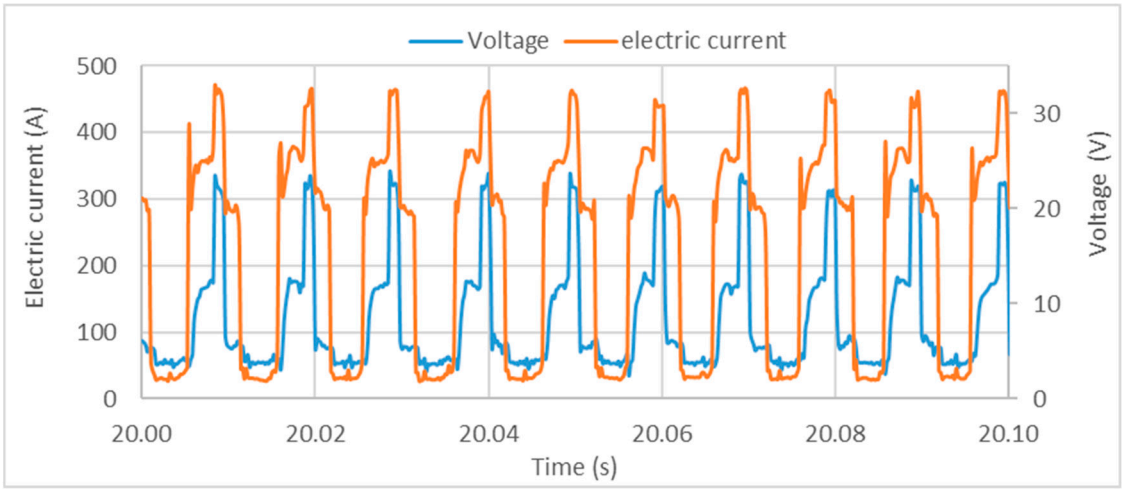

Figure 3. Electric parameters for one welding sequence (during 0.1 s).

The effective current or voltage represents the value of direct current or voltage that yields the same power dissipation due to the Joule effect in a resistive circuit.

$$Es = \frac{P\, t_{arc}}{L} \text{ or } Es = \frac{E_{tot}}{L} \quad (2)$$

With: Es: welding energy (kJ/mm);
P: Average power (kW);
t_{arc}: arc-on time (s);
L: weld length (mm);
E_{tot}: cumulative energy (kJ).

Voltage and current measurements were thus monitored during the welding process, and these measurements provided the curves depicted in Figure 3. For voltage monitoring, a differential probe was used, specifically the MX9030 by Chauvin-Arnoux (Meyzieu, France). This probe was connected to the welding circuit, with a measurement location that was carefully selected to be as close to the welding arc as possible. One connector was affixed to the conductor guide positioned between the torch pusher roller and the contact tube, while the other connector was attached to the generator ground cable.

A Chauvin-Arnoux PAC 21 current clamp was used to monitor the welding current. This PAC 21 clamp was positioned on the ground cable and operates based on the Hall effect principle. The acquisition of voltage and current signals was carried out using a National Instrument CompactRIO system. Our data collection encompassed a total of 60,000 measurement points, with an acquisition time of 60 s and a sampling period of 0.001 s.

The primary contributors to the induced heat cycle are the energy effectively conveyed to the workpiece and the initial temperature, and these factors take precedence regardless of the material physical characteristics.

Nevertheless, owing to several forms of dissipation, including radiation, convection, and conduction losses, the energy furnished by the electric arc is never entirely transferred to the workpiece. Consequently, not all of the thermal energy is transferred to the workpiece during the welding process, as a portion of it is lost through conduction within the wire guides and wire sheaths.

The calculation of heat input, denoted as Q, can be expressed as follows:

$$Q = \eta Es \quad (3)$$

η: Process thermal efficiency coefficient, considered to be 0.8 for the CMT process.

The use of an amperemeter for measuring current intensity and a voltmeter for measuring voltage allowed us to determine the effective welding energy transferred to the workpiece over a specific duration, as demonstrated in the example Figure 3. Additionally, these measurements facilitated the estimation of the heat input and the actual average power absorbed by the sheets in various butt configurations, such as the 1 mm/1 mm and 1.2 mm/1 mm configurations, as detailed in Table 1.

Table 1. Heat input and welding power.

Configuration	1 mm/1 mm	1.2 mm/1 mm
Welding energy *Es* (kJ/mm)	0.242	0.235
Average power *P* (kW)	2.62	2.55
Coefficient η	0.8	0.8
Heat input *Q* (kJ/mm)	0.194	0.188
Average real power (kW)	2.1	2.04

Figure 4 presents the macroscopic cross-sectional views achieved through the process for butt-end configurations. It provides an overview of the macrographs for the two test cases. It is evident that both welding conditions exhibit complete penetration. Furthermore, it is noticeable that the heat input *Q* required to melt the base metal in these two tests is nearly identical. Specifically, since both tests involve a 1 mm thickness on one side, the welding parameters are consistent, ranging from 0.188 kJ/mm to 0.196 kJ/mm. This translates to a negligible relative difference of less than 3%.

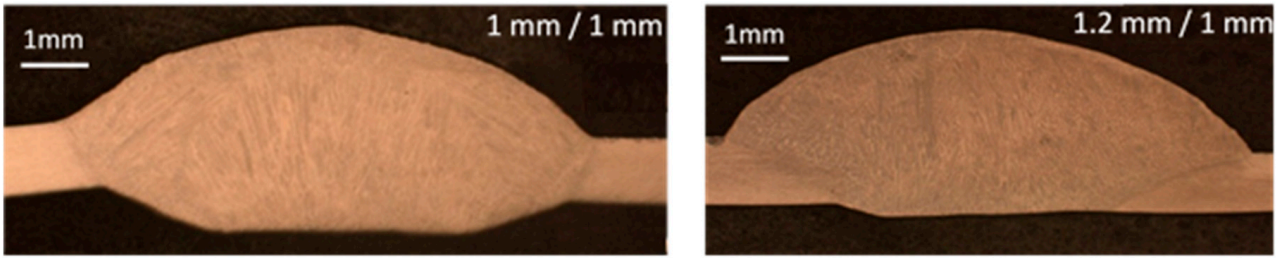

Figure 4. Macrographic sections of the weld.

However, it can also be seen that the use of almost-identical welding parameters resulted in two different seam geometries: the lower joint surfaces have a smaller radius of curvature due to the greater thermal pumping (contact with the copper lath), and the MZ surface of the 1 mm/1 mm configuration is larger than that of the 1.2 mm/1 mm configuration due to the quality of the contact with the copper lath.

Figure 5 and Table 2 depict the schematic and average numerical values of the macrographic measurements for the weld seam dimensions in the context of these two tests. It is worth noting that, in addition to penetration and width, there are several other dimensions to consider in the cross-section of the joint. h, H, l, L, and e represent distinct weld seam dimensions, whereas e_1 and e_2 are the sheet thicknesses.

Table 2. Numerical values of macrographic measurements to be applied for both welds.

Configurations	L (mm)	l (mm)	H (mm)	h (mm)	e (mm) = H + h + e_1
1 mm/1 mm	8.05	7.08	1.43	0.57	3
1.2 mm/1 mm	7.51	5.83	1.52	0.36	3.1

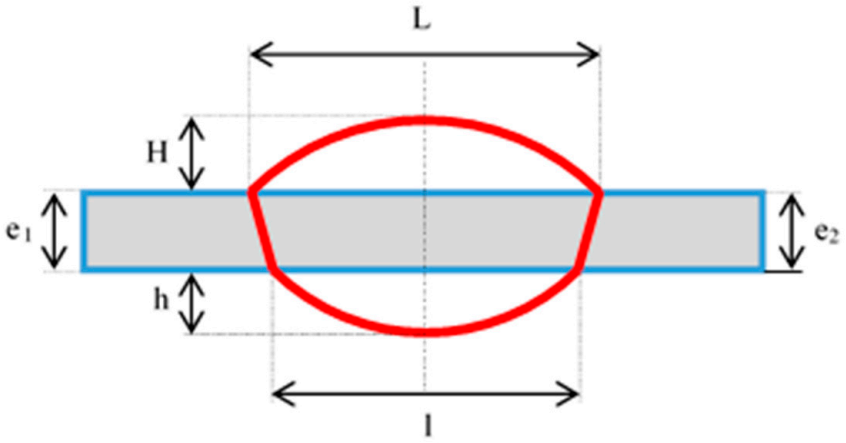

Figure 5. Schematic of macrographic measurements (weld seam dimensions).

The maximum depth difference (e) of the MZ between the two configurations amounted to 0.1 mm. In the 1 mm/1 mm case, both the upper (L) and lower (l) widths of the melted zone were slightly greater than those observed in the 1.2 mm/1 mm configuration. This difference can be explained by a slight, non-significant difference in the average real power absorbed for the two configurations.

3. Numerical Model

In order to establish a comparison between simulations and experiments, this section presents the numerical model used to simulate actual welding experiments using the finite element method (FEM), taking into account initial and boundary conditions. Corresponding thermomechanical calculations were then performed using an equivalent heat source approach.

The simulation results obtained using this approach allowed for determination of the evolution of temperature during welding, as well as evaluation of the deformations and angles of the sheets distortion resulting from the welding operations.

The "heat source identification" and "thermomechanical calculations" sections are based on numerical simulation and experimentations. The equivalent heat sources were identified for both selected end-to-end configurations.

The calculation of deformations requires identification of a behavior law for both the base material and the molten zone. These laws were obtained from the literature [14–16].

In the chosen approach, the stages of numerical simulation of welding involve, firstly, using the geometric and energy parameters to identify an equivalent heat source for each configuration. Secondly, simulated temperature fields during heating and cooling are compared to those obtained experimentally. The next step is to determine the displacements/deformations of the metal sheets from the thermomechanical calculations.

3.1. FEM Model

The finite element (FE) mesh size was chosen on the basis of the literature comparable to our study [17–20]. In order to reduce calculation times, the mesh was defined, including two transition zones 1 and 2 along the transverse direction. To optimize calculation time and accuracy, the size of elements was finer in and around the MZ and HAZ (Heat Affected Zone). On the other hand, elements became coarser away from the weld zone. In the direction of the weld axis, the mesh size was 0.25 mm.

In the weld zone, eight elements were used across the sheet thickness, providing an element size of 0.125 mm. A first transition zone allowed to increase the size element to 0.25 mm (i.e., four elements in the thickness, label 1). Similarly, a second transition zone allowed to use only 2 elements in the thickness (i.e., size element of 0.5 mm in thickness, label 2) sufficiently far away from the weld axis.

Thus, the mesh became coarser between zone 1 and 2 based on the progressive refinement along the lateral lines outside the weld seam. The minimum mesh size in the thickness was 0.125 mm whereas the maximum one was 0.5 mm.

The FE model, including two transition zones and a progressive refinement along the lateral lines, is shown in Figure 6, and it is inspired by the literature [21,22].

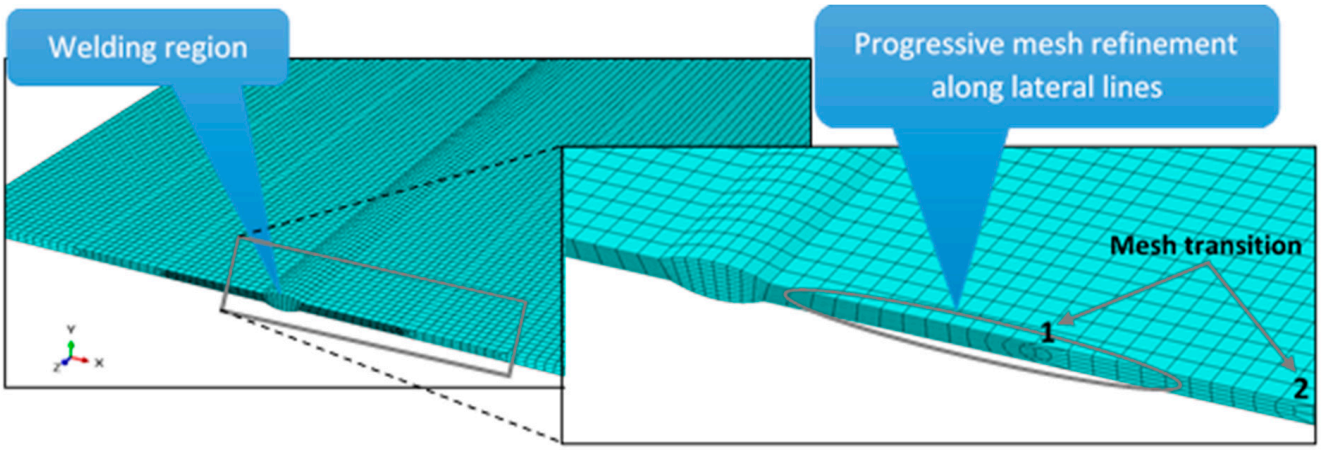

Figure 6. Local model: mesh and welding region.

The use of these transition zones allowed for reduction of the number of elements and nodes, as detailed in Table 3.

Table 3. Number of nodes and mesh elements.

Configurations	Number of Nodes	Number of Elements
1 mm/1 mm	56,762	47,100
1.2 mm/1 mm	58,782	48,800

An isostatism condition was considered for the mechanical boundary conditions, and C3D8RT elements were used as suggested in the literature review [19,23,24]. This type of element (3D bricks with eight nodes) is suitable for thermomechanical calculations.

Within ABAQUS, the steps employed in the current study were categorized into three groups, as detailed in Table 4. The first group of steps was used to apply initial conditions and clamping, which consisted of two steps; the second group was used to simulate progressive activation of elements, and the number of steps corresponded to the number of group of elements, e.g., 25 steps for 25 groups of elements; finally, the last group was used for debriding and cooling, which consisted of a single step. Thermomechanical properties (Poisson's ratio, Young's modulus, yield strength, density, specific heat, thermal conductivity, latent heat of fusion, solidus and liquidus temperatures) as a function of temperature were taken from the literature [22,25,26].

Table 4. Details of calculation steps.

Group of Steps	Number of Steps	Time Step (s)
1. Initial conditions and clamping	2	10^{-5}
2. Simulate progressive activation of elements	25	0.37
3. Debriding and cooling	1	500

Several values of the heat exchange coefficient h were applied to investigate its effect on the maximum predicted temperature. An adjustment of the heat exchange coefficient was hence performed in order to provide the best fit between experimental and calculated temperatures. Finally, the selected coefficient h takes into account both convection and radiative contributions.

For this, values of h ranging between 10 and 60 $W \cdot m^{-2} \cdot {}^{\circ}C^{-1}$ were tested. The choice of welding on a copper lath was made in view of the very-low thickness of the sheets to be welded. It is essential to avoid any risk that the weld pool collapses when assembling this type of sheet. Copper was also chosen because it cools the weld pool very quickly, thus avoiding oxidation problems on the reverse side of the weld seam.

A Bilinear Isotropic Strain Hardening Model was selected to set up the elastoplastic behavior for the base material and molten zone. This type of model allows for consideration of the dependence of properties (Young's modulus E, tangent modulus E_t, and yield stress σ_e) on temperature. The plastic strain ε_{pl} was determined from the literature data [24] obtained from experimental nominal stress-nominal strain curves, see Figure 7.

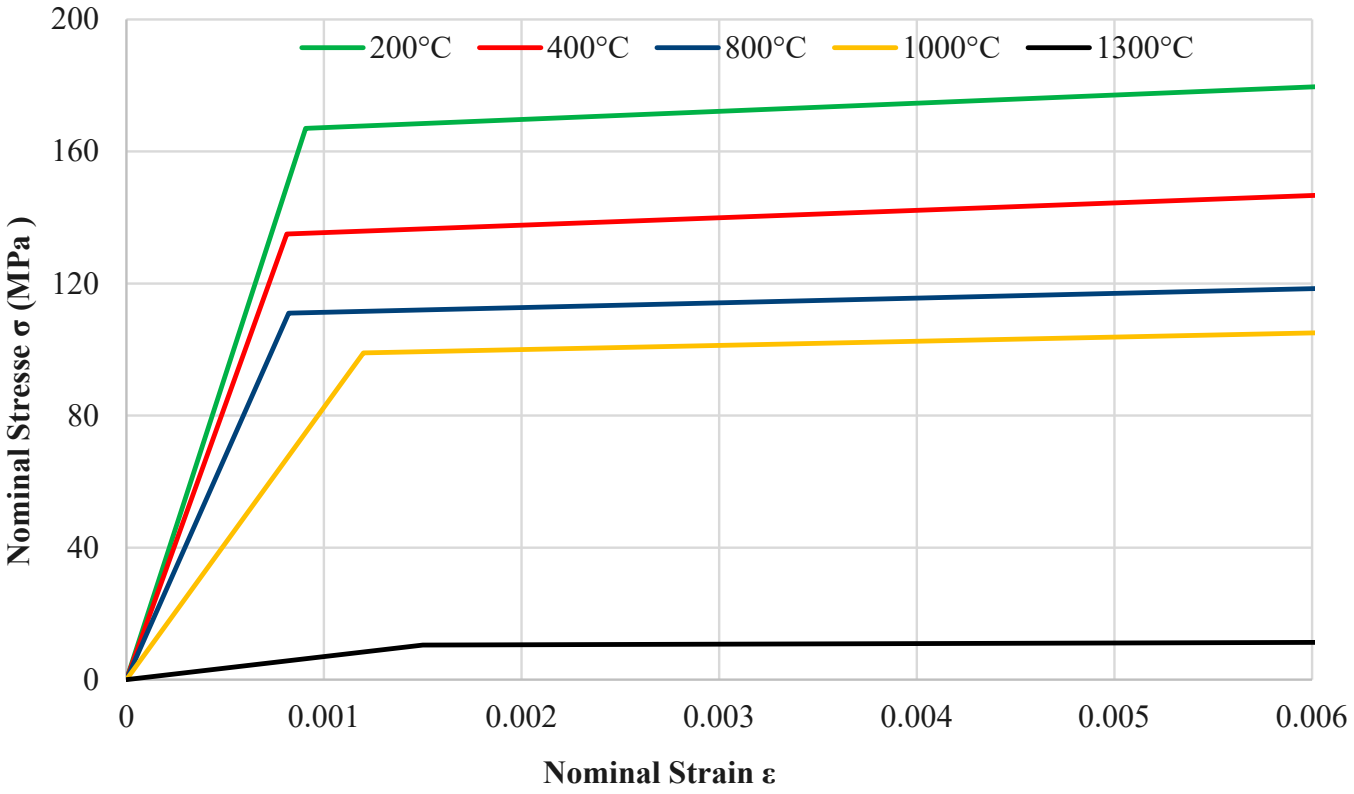

Figure 7. Mechanical properties of 304L stainless-steel for the bilinear isotropic strain hardening model [24].

This type of behavior law includes three material parameters that are necessary for the calculation: E, E_t, and σ_e. The strain-hardening parameter μ represents the ratio between the E_t and the E.

A sensitivity study was carried out by Akbari Mousavi [14] and Brickstad [15] in order to determine the value of μ for 304L and 316L stainless-steels at different temperatures T and to assess the influence of varying this value on the obtained final deformation. Finally, the μ ratio was set to 0.0133 for temperatures up to 800 °C, and to 0.0001above 800 °C.

In the present work, the elastoplastic behavior model of 316L stainless-steel was assumed to be identical to that of 304L, since Young's moduli as a function of temperature are almost identical [21,22,27].

In ABAQUS software (version 2018), thermal strains are determined by the following mathematical formula:

$$\varepsilon_{th} = \int_{T_{ref}}^{T} \alpha_T dT - \int_{T_{ref}}^{T_{init}} \alpha_{init}\, dT = \overline{\alpha_T}\left(T - T_{ref}\right) - \overline{\alpha_{init}}\left(T_{init} - T_{ref}\right) \quad (4)$$

With:

ε_{th}: Thermal strain;
$\overline{\alpha_T}$: Average coefficient of thermal expansion at a current temperature (°C^{-1});
T: Current temperature (°C);
$\overline{\alpha_{init}}$: Average coefficient of thermal expansion at an initial temperature (°C^{-1});
T_{init}: Initial temperature (°C);
T_{ref} : Metal reference temperature (°C).

The reference temperatures T_{ref} for the base metal and seam metal used in our calculations are 25 °C (ambient temperature) and 1450 °C (melting temperature), respectively.

The ABAQUS "NLGEOM" parameter was used to activate the large deformations option since the small deformation option was found to provide non-realistic results.

Residual deformations induced by the sheet manufacturing process, e.g., rolling, were not considered. It was assumed that, at the melting point of the material, local plastic deformation was suppressed and new plastic deformation was prevented after melting (i.e., the transition from liquid to solid state), so that the material was reconstructed and the history of the material was assumed to be erased locally under the effect of previous treatments [28].

It was assumed that the weld seam was divided into several elements of equal length, which were activated progressively during welding.

This was simulated using the "Element Birth and Death" technique available within ABAQUS and well explained in [29–31]. The elements were considered inactive at the beginning of welding process, i.e., "dead" at the start of the calculation. They were then activated as the heat source progresses, i.e., "birth". This technique is adopted to simulate a real welding process, as the seam was formed by a mixture of base metal and filler metal. A quantity of filler metal material was deposited evenly as the filler wire melted. The filler metal was modeled by the progressive activation of elements of a previously meshed seam. This approach assumes that the geometry of the seam is known before the calculation is carried out (geometry of the equivalent heat source, see Figure 5 and Table 2).

3.2. Equivalent Heat Source Approach

An equivalent heat source approach was adopted, with an imposed cross-section propagated along a length L_w in the direction of the seam axis. The cross-section was made up of two disc-segments separated by an intermediate trapezoid; therefore, it was a prismatic type source. The elements were progressively activated during calculations, and the source moved linearly in time; an example is shown in Figure 8. Note that L_w represents the optimum value for element length, for which calculation results close to reality have been obtained.

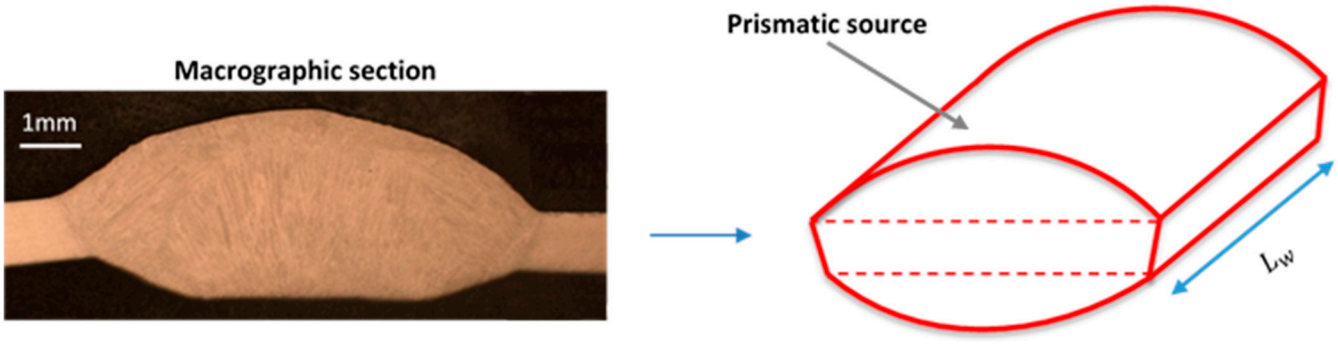

Figure 8. Prismatic source composed of a trapezoid and two disc segments.

This source was used to represent the distribution of absorbed energy across the thickness of the sheets. Temperature fields were calculated, considering thermal convection effects. The initial temperature of the sheets was 25 °C, and an overall heat exchange coefficient was considered, as elaborated earlier. Finally, the coupling between the thermal problem and the mechanical one was weak.

This approach, which enables the shape of the molten zone to be represented, was implemented in a DFLUX subroutine coded in FORTRAN. It takes the history of elements into account, which includes changes from solid to liquid states, and from liquid to solid. It also takes the actual geometry of the seams into account, which varies strongly with the filler material addition, as suggested in Figure 4.

A three-dimensional thermomechanical model was developed to calculate deformations for a suitable equivalent volumetric heat source. A welding speed of 0.65 m/min was considered, as well as the average real power input provided for each configuration homogeneously distributed in the volume of the prismatic source as shown on Figure 8.

4. Results and Discussions

This section presents the FE results of the thermal and mechanical simulations applied to previously described experiments. A comparative analysis of thermal and mechanical results computed for each configuration is performed. In addition, temperature measurements and digital image correlation results are compared to the predicted temperatures and displacement fields. Finally, the measured deformation angles are compared to the predicted ones.

Comparison between the experimental macrostructure of the weld bead and the predicted geometry of the MZ for the two different welding cases is shown in Figure 9.

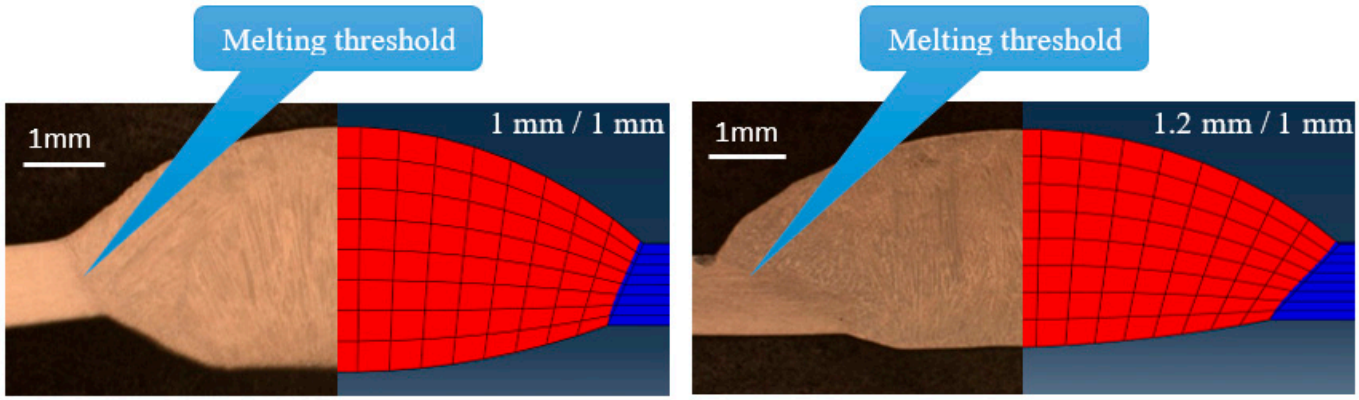

Figure 9. Comparison between experimental macrostructure and shape of predicted molten zone MZ.

Table 5 summarizes the maximum temperatures recorded by TC_0 and TC_1 thermocouples on the assembly shown in Figure 1, i.e., thermocouples placed at 20 mm from the weld seam. The maximal temperatures recorded do not exceed 260 °C for the 1 mm/1 mm configuration and 340 °C for the 1.2 mm/1 mm configuration due to the increase in the conductive thermal resistance between the TC measurement point and the copper lath. Temperatures then dropped progressively to ambient temperature.

Table 5. Maximum temperatures measured by thermocouples placed at 20 mm from the weld line.

Configurations	Thickness (mm)	Maximum Measured Temperature (°C)
1 mm/1 mm	1 1	254
1.2 mm/1 mm	1.2 1	335 272

Despite the welding parameters being almost identical for the two configurations (power, wire feed rates, and welding speeds), when linearly approximating the heating and cooling phases on the graphs shown in Figures 10 and 11, it is clear that the average heating and cooling rates for the 1 mm/1 mm configuration (12.95 °C/s and 0.47 °C/s, respectively) are lower than those for the 1.2 mm/1 mm configuration (28.57 °C/s and

0.51 °C/s). This might be correlated to the higher cross-sectional area of the MZ in the former configuration (17.9 mm^2) in comparison with the latter one (17 mm^2).

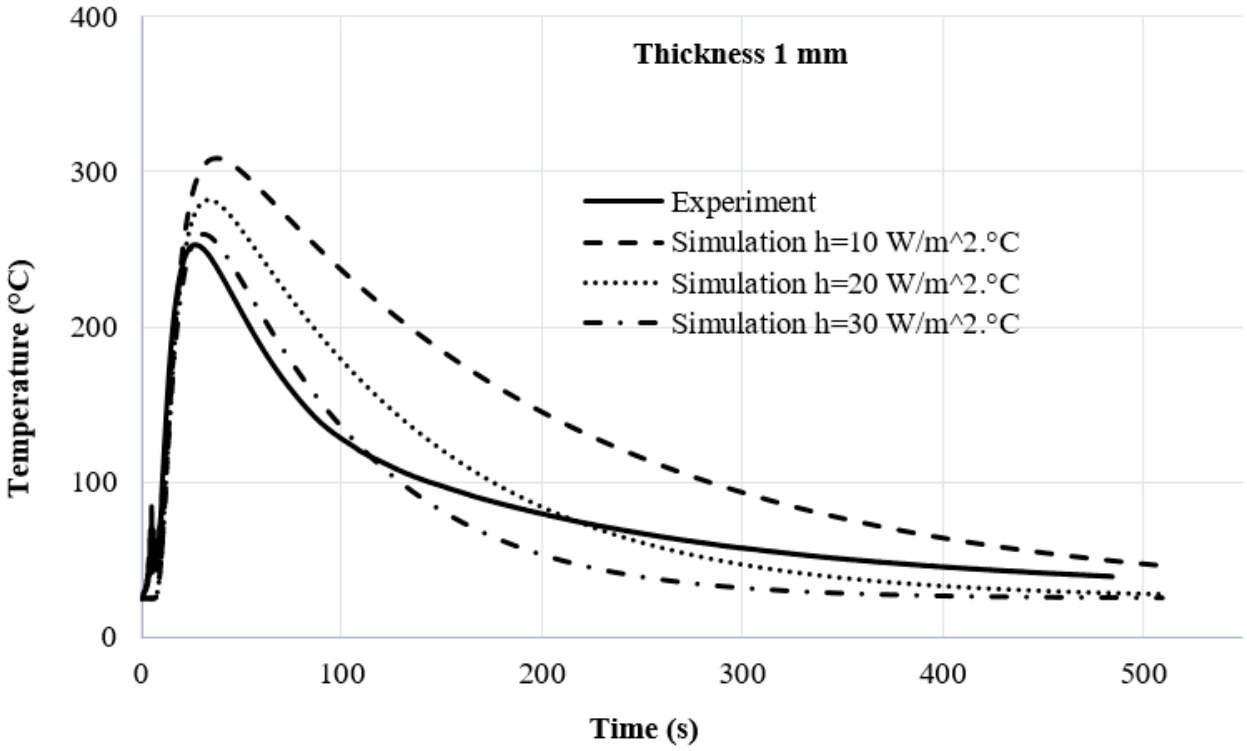

Figure 10. Thermal parametric study: temperature at 20 mm from the seam axis for various values of *h*, case 1 mm/1 mm.

In the context of the 1 mm thick sheets, the maximum temperature achieved in the first configuration (1 mm/1 mm) is lower than that recorded in the second configuration (1.2 mm/1 mm): 254 °C for the former compared to 272 °C for the latter.

In the case of the second configuration, the peak temperature reached by the 1.2 mm sheet section exceeds that measured for the 1 mm sheet section, as depicted in Table 5 and Figure 11. These phenomena are likely linked to the presence of the copper lath; in detail, the conductive thermal resistance between the TC measurement point and the copper lath increases by 20% for the 1.2 mm/1 mm configuration.

Figure 10 shows the results of the thermal parametric study for the 1 mm/1 mm configuration. It demonstrates the transient temperature evolution during welding and cooling at a point located 20 mm from the seam axis on the upper surface of the sheet.

The relative difference between the maximum calculated temperatures and those measured in the two parts of the sheet once assembled (thickness 1 mm) is low, which confirms the good correlation, Table 6.

Table 6. Relative difference between measured and calculated maximum temperatures for various values of the *h*, case 1 mm/1 mm.

Convective Heat Transfer Coefficient *h* ($W \cdot m^{-2} \cdot °C^{-1}$)	Relative Difference in the Maximum Temperatures (%)
10	22
20	11.3
30	2.6

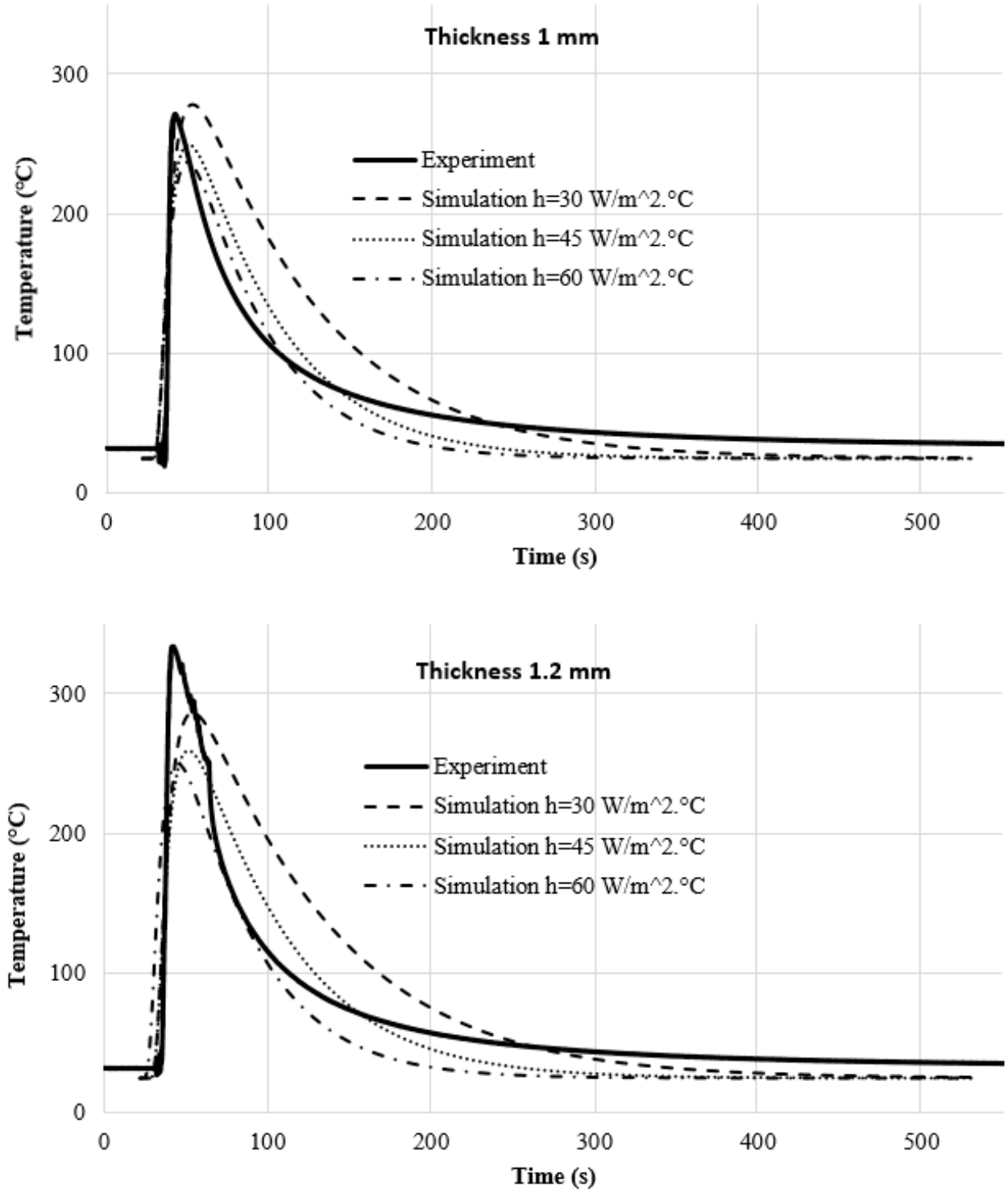

Figure 11. Thermal parametric study: temperature at 20 mm from the seam axis for various values of h, case 1.2 mm/1 mm.

The maximum temperature calculated with a heat exchange coefficient $h = 30\ W{\cdot}m^{-2}{\cdot}{}^{\circ}C^{-1}$ provides a smaller relative difference compared to other values of the heat exchange coefficient (this difference is lower than 3%).

Comparison between experimental results and the computed ones, according to variable heat exchange coefficients chosen beforehand: h = 10, 20 and 30 $W{\cdot}m^{-2}{\cdot}{}^{\circ}C^{-1}$, provide a satisfactory comparison for $h = 30\ W{\cdot}m^{-2}{\cdot}{}^{\circ}C^{-1}$, and higher differences for h = 10 and 20 $W{\cdot}m^{-2}{\cdot}{}^{\circ}C^{-1}$.

Figure 11 exhibits the results of the thermal parametric study for the 1.2 mm/1 mm configuration. It shines light on the temperature evolution during welding and cooling at a point located 20 mm from the seam axis and on the upper surface of the assembly in both the 1.2 mm and 1 mm thick sheets.

A comparison between experimental results with the computed ones is indicated based on the application of variable values of the h (chosen beforehand among h = 30, 45 and 60 $W{\cdot}m^{-2}{\cdot}^{\circ}C^{-1}$). Again, the comparison yields to satisfactory conclusions for h = 30 $W{\cdot}m^{-2}{\cdot}^{\circ}C^{-1}$ and higher differences for the two other values of h.

The relative difference between the maximum calculated temperature and the measured ones in the 1 mm thick section of the assembly gives results closer to reality (the difference is less than 13% for the three different values of h), see Table 7. In the 1.2 mm thick section, the difference is less than 14% for h = 30 $W{\cdot}m^{-2}{\cdot}^{\circ}C^{-1}$ and greater than this percentage for the other values of h. This can be explained by the loss of contact between the copper lath and the sheet during welding due to induced deformation.

Table 7. Relative differences between measured and calculated maximum temperatures for different values of h, case 1.2 mm/1 mm.

Convective Heat Transfer Coefficient h ($Watt.{\cdot}m^{-2}{\cdot}^{\circ}C^{-1}$)	Relative Difference between the Maximum Temperatures (%)	
	Thickness 1.2 mm	Thickness 1 mm
30	13.7	3.1
45	22.3	8
60	25.1	12.7

Finally, the heat transfer coefficient retained for both calculations was thus h = 30 $W{\cdot}m^{-2}{\cdot}^{\circ}C^{-1}$. This coefficient is justified by the fact that CMT was performed on metal sheets in direct contact with a copper lath, and also by the fact that it also includes radiative losses.

Using the equivalent heat source approach for the thermo-mechanical calculation enabled us to make a comparison between the computed results and experiments at the deformation level.

An example of the results of calculated displacements (U2 or V) in the Y direction, normal to the sheet surface, after welding, case 1 mm/1 mm, is shown in Figure 12. The overall deformation may be observed, and estimates of the deformation angle of the sheet after cooling may be derived. The same type of overall deformation is observed in both cases: the assembly takes on the shape of horse saddle.

In order to measure the deformation angle at the sheet ends, extraction of the vertical displacement profile (V) was performed for two lines L_0 along the sheet width direction (X), see Figure 12.

Figure 13 shows the comparison between experiments (DIC measurements line L_0) and simulations for the vertical displacements (V) along the width (line L_0). The measurements and calculations show similar concave curvatures.

Comparison of the thermomechanical calculation results with experimental ones for the two cases yielded satisfactory conclusions for the cross-sectional direction of the sheet (80 mm), i.e., for the 1 mm/1 mm case.

The calculated deformation angle is close to the real angle, which is around 2.7°, and the difference between calculation and experiments being around 0.3°. For the 1.2 mm/1 mm case, the difference between calculation and experiments is 0.1° for the 1 mm thick coupon and 0.3° for the 1.2 mm thick coupon, see Table 8.

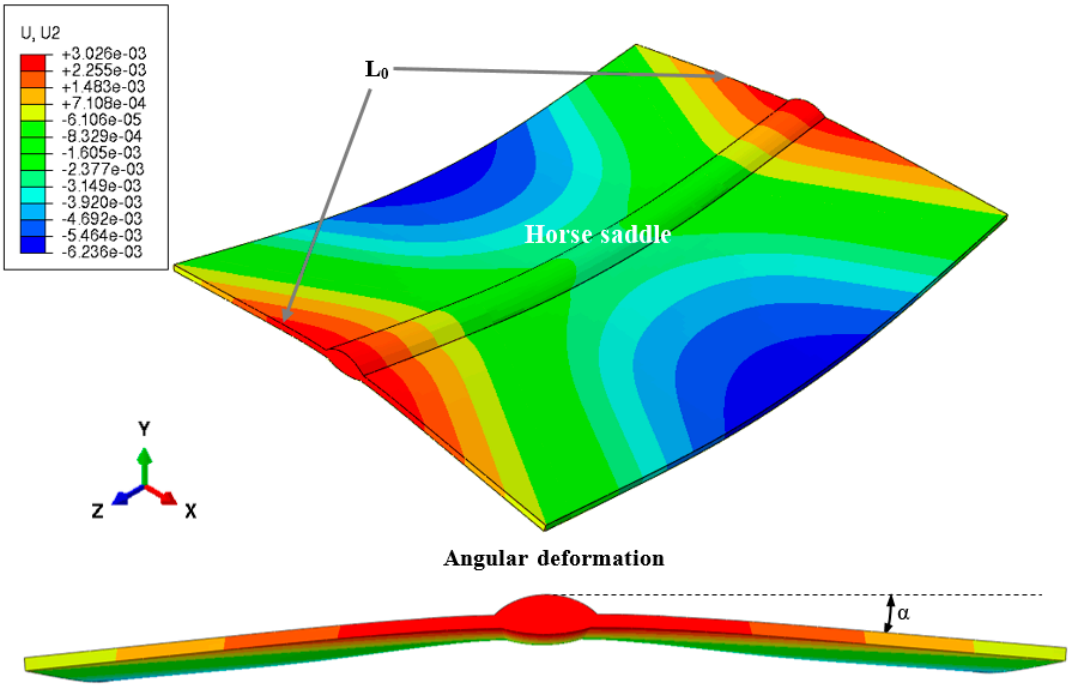

Figure 12. Numerically calculated displacements and deformation shape, case 1 mm/1 mm.

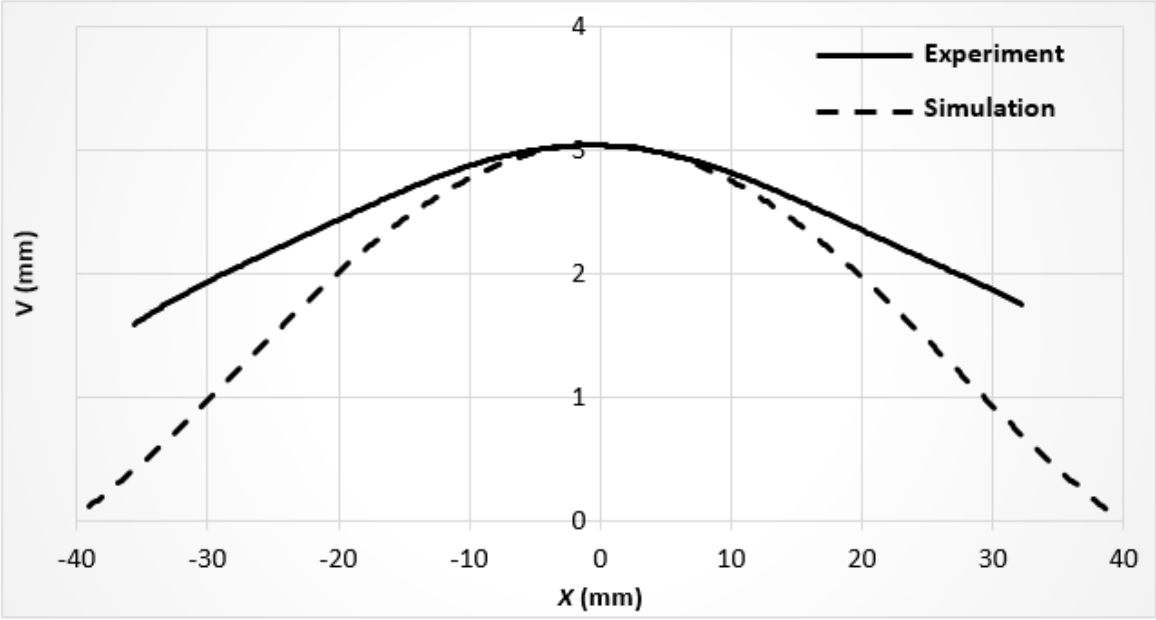

Figure 13. Comparison between computed results and DIC displacements along line L_0, case 1 mm/1 mm.

Table 8. Comparison of calculated (FEM) and measured (DIC) deformation angles along line L_0.

Configurations	Experiment		Simulation	
1 mm/1 mm	1 mm 2.7°	1 mm 2.8°	1 mm 3°	1 mm 3°
1.2 mm/1 mm	1.2 mm 4.9°	1 mm 6.1°	1.2 mm 5°	1 mm 5.8°

Vertical displacement amplitudes and deformation angles at the ends of the thickest coupons were greater than those of thinner sheets, see Figures 13 and 14 and Table 8. Increasing the thickness of the second coupon therefore increases displacements, deformations, and deformation angles. On the contrary, the thinner the sheets are, the smaller the deformations generated for the present conditions.

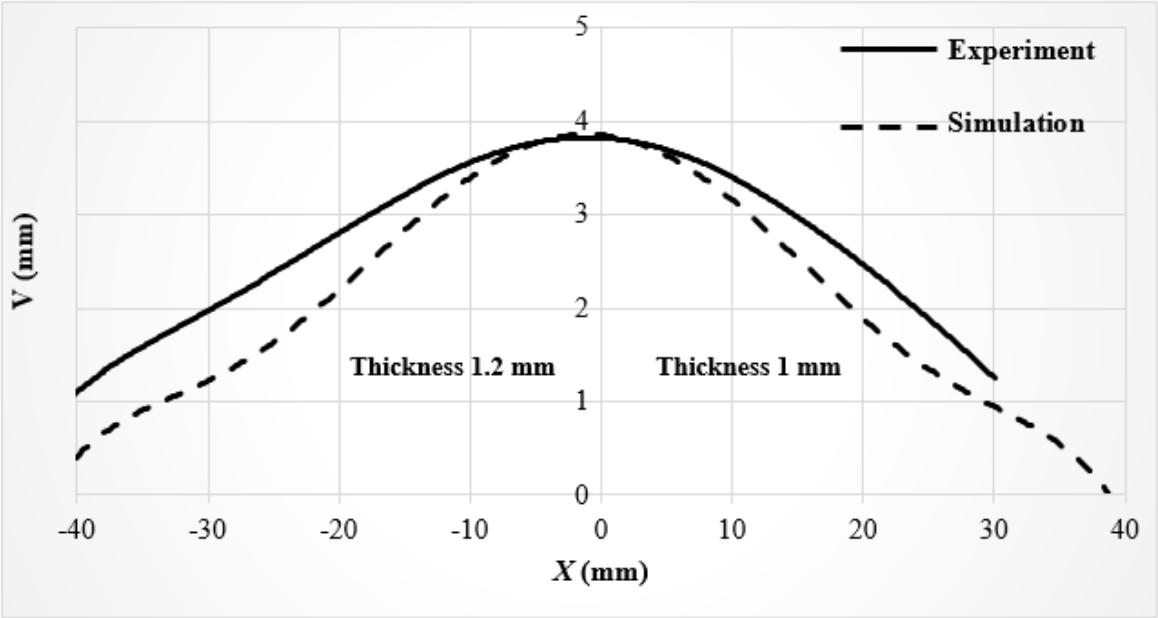

Figure 14. Comparison between computed results and DIC displacements along line L_0, case 1.2 mm/1 mm.

This can be explained by observation of the macrographs, where there is competition between the two dimensions L (upper dimension of weld bead width) and l (lower dimension of weld bead width), see Figure 5 and Table 2. In both cases, the L dimension is greater than the l dimension. The difference between the two dimensions (L-l) in the 1.2 mm/1 mm case is around 2 mm, which is greater than that in the 1 mm/1 mm case, which leads us to say that the greater the difference is, the greater the displacements and deformation angles are. In other words, the more the weld beam is dissymmetric in regard to the thickness direction, the higher the deformations are.

5. Conclusions

The two heat sources, as well as the heat exchange coefficient identified in these studies, have been implemented in a thermomechanical simulation of the assembly operation of two sheets of stainless-steel 304L in two butt welding configurations, namely 1 mm/1 mm and 1 mm/1.2 mm, representing the project's areas of interest for which the work presented here was funded. The main challenge associated with implementing the thermomechanical calculation is related to the meshing of the calculation domain representing a thin metal sheet. The minimum size of the elements, and therefore the quality of the mesh, is linked to the thickness of the sheet. To limit the number of degrees of freedom of the problem to be solved while maintaining sufficient calculation accuracy, transition zones were used between the finely meshed weld seam zone and the rest of the coupon, which experienced lower thermal and mechanical gradients. With this choice, the results obtained agree with experimental observations; the relative difference between the measured temperatures and the calculated ones is less than 5%, and the relative difference between the calculated and observed angular distortion is less than 10%. This lesser consideration of the distortion effect by the model is linked to the considered conditions to simulate the clamping of the sheet and the pointing before welding. In the experiments, welding was performed after pointing, where the sheet was clamped and then released immediately after welding to

allow for the sheet to deform freely. In the calculation, the sheets were considered free to deform even during welding, which was not possible to achieve experimentally. This explains the slight overestimation of the calculated distortion angle, but the offset is limited and the model accurately reproduces the behavior in terms of distortion of the welded coupon. These initial works were useful for the modeling of a real structure, i.e., a 1/4 scale prototype of a tanker for road transport. In the case of a real structure, the sheets are self-clamped, and the overall structure is free to deform; thus, the simulated clamping conditions are more representative of a real structure welding scenario. Therefore, we believe that the model is satisfactory for our ultimate goal of simulating a real structure.

The final objectives of this work, namely the comparison between the experimental and calculated results for plates welded in butt configuration using the CMT process, have been achieved. By identifying and modeling an equivalent heat source, simulation of the thermal and thermomechanical behaviors of the produced assembly was achieved.

The approach used in the simulation step may help to solve a wide range of problems, including:

- Determining angular distortion within the welded structure.
- Analyzing displacement fields of the welded plates.
- Studying the transient evolution of temperature in proximity to the welding zone.
- Determining the maximum temperatures reached on a specific sheet during the welding process.

The simulation produced satisfactory outcomes, aligning with the experimental findings. Although simulation is advantageous, it falls short of completely substituting experimentation. The careful selection of experimental test cases that are easy to simulate is pivotal. Simulating a fine assembly on a copper lath is notably intricate due to the necessity of replicating the contact between the assembly and the copper lath.

The models developed in this study merit further exploration in the future and can be extended to cover materials of different thicknesses and various CMT welding configurations. In addition, these models can be used to develop a simplified approach capable of simulating the deformation of large-scale structures.

Author Contributions: Methodology, A.M. and R.B.; Validation, F.L.; Resources, L.B.; Writing—original draft, H.A.; Visualization, N.H. and A.C. All authors have read and agreed to the published version of the manuscript.

Funding: This research received no external funding.

Data Availability Statement: Data are contained within the article.

Acknowledgments: The financial support of ADEME (Agence de l'Environnement et de la Maîtrise de l'Energie) throughout the LightTank project is acknowledged.

Conflicts of Interest: Author Hichem ABERBACHE was employed by the company MAGYAR-SMFF and Laboratoire Interdisciplinaire Carnot de Bourgogne. The remaining authors declare that the research was conducted in the absence of any commercial or financial relationships that could be construed as a potential conflict of interest.

Nomenclature

E_s	Linear welding energy (kJ/mm)
U	Voltage (V)
I	Current (A)
V_w	Welding velocity (mm/min)
P	Average power (kW)
t_{arc}	Arc-on time (s)
L_w	Weld length (mm)
E_{tot}	Cumulative energy (kJ)
Q	Heat input (kJ/mm)
η	Process thermal efficiency coefficient

E	Young's modulus (GPa)
E_t	Tangent modulus (GPa)
σ_e	Yield stress (MPa)
μ	Strain hardening
h	Heat exchange coefficient ($W \cdot m^{-2} \cdot °C^{-1}$)
ε_{pl}	Plastic deformation
ε_{th}	Thermal strain
T	Current temperature (°C)
α_T	Thermal expansion coefficient ($°C^{-1}$)
$\overline{\alpha_T}$	Average coefficient of thermal expansion at a current temperature ($°C^{-1}$)
$\overline{\alpha_{init}}$	Average coefficient of thermal expansion at an initial temperature ($°C^{-1}$)
T_{init}	Initial temperature (°C)
T_{ref}	Metal reference temperature (°C)
X, Y, Z	Subscripts (Cartesian coordinates)

References

1. Fronius International. Available online: http://www.fronius.com/en (accessed on 27 July 2023).
2. Wesling, V.; Schram, A.; Kessler, M. Low heat joining—Manufacturing and fatigue strength of brazed, locally hardened structures. *Adv. Mater. Res.* **2010**, *137*, 347–374. [CrossRef]
3. Furukawa, K. New CMT arc welding process—Welding of steel to aluminium dissimilar metals and welding of super-thin aluminium sheets. *Weld. Int.* **2010**, *20*, 440–445. [CrossRef]
4. Matusiak, J.; Pfeifer, T. The research of technological and environmental conditions during low-energetic gas-shielded metal arc welding of aluminium alloys. *Weld. Int.* **2011**, *27*, 338–344. [CrossRef]
5. Nishimura, R.; Ma, N.; Liu, Y.; Li, W.; Yasuki, T. Measurement and analysis of welding deformation and residual stress in CMT welded lap joints of 1180 MPa steel sheets. *J. Manuf. Process.* **2021**, *72*, 515–528. [CrossRef]
6. Talalaev, R.; Veinthal, R.; Laansoo, A.; Sarkans, M. Cold metal transfer (CMT) welding of thin sheet metal products. *Est. J. Eng.* **2012**, *18*, 243–250. [CrossRef]
7. CMT (Cold Metal Transfer) de FRONIUS, une Nouvelle Technologie de Soudage à L'arc Qui Ouvre de Nouvelles Perspectives. Available online: https://www.machine-outil.com/actualites/t154/a1250-cmt-cold-metal-transfer-de-fronius-une-nouvelle-technologie-de-soudage-a-l-arc-qui-ouvre-de-nouvelles-perspectives.html (accessed on 10 June 2023).
8. Azar, A.S. A heat source model for cold metal transfer (CMT) welding. *J. Therm. Anal. Calorim.* **2015**, *122*, 741–746. [CrossRef]
9. Wu, K.; He, Z.; Dong, Z.; Lan, Y. Numerical simulation of the temperature field of cold metal transfer welding pool. *Mechanika* **2016**, *22*, 285–290. [CrossRef]
10. Rao, Z.; Li, Y.; Liu, J.; Liao, S.M.; Wang, F. Numerical simulation of heat and mass transfer during CMT welding of aluminum alloy and galvanized mild steel. *J. Manuf. Sci. Eng.* **2015**, *136*, 108530. [CrossRef]
11. Escribano-García, R.; Rodriguez, N.; Zubiri, O.; Piccini, J.; Setien, I. 3D numerical simulation of GMAW Cold Metal Transfer using response surface methodology. *J. Manuf. Process.* **2022**, *76*, 656–665. [CrossRef]
12. Cambon, C.; Rouquette, S.; Bendaoud, I.; Bordreuil, C.; Wimpory, R.; Soulie, F. Thermo-mechanical simulation of overlaid layers made with wire + arc additive manufacturing and GMAW-cold metal transfer. *Weld. World* **2020**, *64*, 1427–1435. [CrossRef]
13. Schreier, H.; Orteu, J.-J.; Sutton, M.A. *Image Correlation for Shape, Motion and Deformation Measurement*; Springer Science: Berlin/Heidelberg, Germany, 2009; p. 322. [CrossRef]
14. Mousavi, S.A.; Miresmaeili, R. Experimental and numerical analyses of residual stress distributions in TIG welding process for 304L stainless steel. *J. Am. Acad. Dermatol.* **2008**, *208*, 383–394. [CrossRef]
15. Brickstad, B.; Josefson, B. A parametric study of residual stresses in multi-pass butt-welded stainless steel pipes. *Int. J. Press. Vessel. Pip.* **1998**, *75*, 11–25. [CrossRef]
16. Tchoumi, T.; Peyraut, F.; Bolot, R. Influence of the welding speed on the distortion of thin stainless steel plates—Numerical and experimental investigations in the framework of the food industry machines. *J. Mater. Process. Technol.* **2016**, *229*, 216–229. [CrossRef]
17. Huang, H.; Wang, J.; Li, L.; Ma, N. Prediction of laser welding induced deformation in thin sheets by efficient numerical modeling. *J. Mater. Process. Technol.* **2016**, *227*, 117–128. [CrossRef]
18. Ma, N.; Li, L.; Huang, H.; Chang, S.; Murakawa, H. Residual stresses in laser-arc hybrid welded butt-joint with different energy ratios. *J. Mater. Process. Technol.* **2015**, *220*, 36–45. [CrossRef]
19. Nagy, M.; Behúlová, M. Design of welding parameters for laser welding of thin-walled stainless steel tubes using numerical simulation. *IOP Conf. Ser. Mater. Sci. Eng.* **2017**, *266*, 012013. [CrossRef]
20. Javadi, Y.; Akhlaghi, M.; Najafabadi, M.A. Using finite element and ultrasonic method to evaluate welding longitudinal residual stress through the thickness in austenitic stainless steel plates. *Mater. Des.* **2013**, *45*, 628–642. [CrossRef]
21. Chukkan, J.R.; Vasudevan, M.; Muthukumaran, S.; Kumar, R.R.; Chandrasekhar, N. Simulation of laser butt welding of AISI 316L stainless steel sheet using various heat sources and experimental validation. *J. Mater. Process. Technol.* **2015**, *219*, 48–59. [CrossRef]

22. Feli, S.; Aaleagha, M.E.A.; Jahanban, M.R. Evaluation Effects of Modeling Parameters on the Tem- perature Fields and Residual Stresses of Butt-Welded Stain- less Steel Pipes. *J. Str. Anal.* **2017**, *1*, 25–33.
23. Zain-Ul-Abdein, M.; Nelias, D.; Jullien, J.-F.; Deloison, D. Prediction of laser beam welding-induced distortions and residual stresses by numerical simulation for aeronautic application. *J. Mater. Process. Technol.* **2009**, *209*, 2907–2917. [CrossRef]
24. Li, Y.; Zhao, Y.; Li, Q.; Wu, A.; Zhu, R.; Wang, G. Effects of welding condition on weld shape and distortion in electron beam welded Ti2AlNb alloy joints. *Mater. Des.* **2017**, *114*, 226–233. [CrossRef]
25. Attarha, M.; Sattari-Far, I. Study on welding temperature distribution in thin welded plates through experimental measurements and finite element simulation. *J. Mater. Process. Technol.* **2011**, *211*, 688–694. [CrossRef]
26. Xu, J.; Chen, J.; Duan, Y.; Yu, C.; Chen, J.; Lu, H. Comparison of residual stress induced by TIG and LBW in girth weld of AISI 304 stainless steel pipes. *J. Mater. Process. Technol.* **2017**, *248*, 178–184. [CrossRef]
27. Tchoumi Nyankam, T.C. Multiphysics Modeling of the Welding arc and the Weld Beat during Welding Operation: Prediction of Distorsions ad Residual Stresses. Ph.D. Thesis, University of Technology of Belfort-Montbéliard (UTBM), Belfort, France, 2016. Available online: https://theses.hal.science/tel-01873488 (accessed on 14 December 2022).
28. Loose, T.; Klöppel, T. An ls-dyna material model for the consistent simulation of welding, forming and heat treatment. In Proceedings of the 11th International Seminar Numerical Analysis of Weldability, Seggau, Austria, 21–24 September 2015.
29. Capriccioli, A.; Frosi, P. Multipurpose ANSYS FE procedure for welding processes simulation. *Fusion Eng. Des.* **2009**, *84*, 546–553. [CrossRef]
30. Fanous, I.F.Z.; Younan, M.Y.A.; Wifi, A.S. 3-D Finite Element Modeling of the Welding Process Using Element Birth and Element Movement Techniques. *J. Press. Vessel. Technol.* **2003**, *125*, 144–150. [CrossRef]
31. Lindgren, L.E. Finite element modeling and simulation of welding part 1: Increased complexity. *J. Therm. Stress.* **2001**, *24*, 141–192. [CrossRef]